Journal of Photochemistry and Photobiology 9 (2022) 100088

Contents lists available at ScienceDirect

Journal of Photochemistry and Photobiology

journal homepage: www.sciencedirect.com/journal/journal-of-photochemistry-and-photobiology

Inhibited interlayer electron transfer in metal ion linked multilayers on mesoporous metal oxide films

Ashley Arcidiacono, Alex J. Robb, Rafael A. Masitas, Sahan R. Salpage, Grace M. McLeod, Jiaqi Chen, Omotola O. Ogunsolu, Michael G. Roper, Kenneth Hanson *

Department of Chemistry & Biochemistry, Florida State University, 102 Varsity Way, Csl 5006, Tallahassee, FL 32306, United States

ARTICLE INFO

Keywords:
Metal ion linked
Multilayer
Dye-sensitized
Electron transfer
Electron donor

ABSTRACT

The incorporation of dye-electron donor motifs on metal oxide surfaces is a common strategy to increase dye regeneration rate, slow recombination, and improve overall dye-sensitized device performance. Here we used zinc ion linked multilayer assembly of a dye (**N3**) and a cobalt polypyridyl electron donor (**Co**) on TiO_2 as an alternative to traditional covalently linked dye-donor systems. The formation of the TiO_2-**N3**-Zn-**Co** multilayer was monitored using UV–Vis and ATR-IR and we introduced inductively coupled plasma mass spectrometry as a means of quantifying the surface loading of spectroscopically obscured molecules like **Co**. Interestingly, and contrary to the original intent, the addition of **Co** electron donor impeded the dye-sensitized device in nearly every performance metric. Transient absorption measurements indicate that both excited state quenching of **N3** by **Co** and **Co** to **N3**$^+$ electron transfer are slower than the intrinsic excited state decay and recombination, respectively. We suggest that the geometric restriction imposed by the metal ion linked architecture sufficiently slows electron transfer such that **Co** is effectively inert in this assembly. While this bilayer did not improve device performance, these insights may guide new design strategies that will improve performance and/or will be of use in other applications where electron transfer is not desired but say communication of spin and/or magnetic moment is needed.

Introduction

Ease of fabrication, flexibility, and low cost make dye-sensitized devices an intriguing architecture for converting sunlight into electrical and chemical energy in dye-sensitized solar cells (DSSCs) [1] and dye-sensitized photoelectrochemical cells (DSPECs) [2], respectively. In these devices, excitation of the dye is followed by electron injection (k_{inj} in Fig. 1) into the conduction band of a metal oxide substrate. The oxidized dye can then be reduced (i.e. regenerated, k_{reg}) by either an electron donor or catalyst. Ideally, the electron in the conduction band then enters the external circuit to generate electricity or reduce a substrate to form chemical fuels. However, the electron in the conduction band can also be non-productively lost via back electron transfer to the oxidized dye (k_{BET}) or through recombination with the oxidized donor on the surface or in solution (k_{rec}). In a DSPEC, k_{BET} and k_{rec} must be slowed by several orders of magnitude for the solar flux-limited buildup of redox equivalents for catalysis to be competitive with these loss pathways [3]. Likewise, in DSSCs, slowing k_{BET} and k_{rec} by one order of magnitude can increase the open-circuit voltage by 50 mV or more [4].

Covalently linking an electron donating moiety to the dye is a popular strategy to increase k_{reg} and spatially separate the oxidized equivalent away from the metal oxide surface, slowing k_{BET} and k_{rec} [5,6]. This strategy is effective but typically requires complex multi-step syntheses to generate the covalently linked dyad. Metal-ion linked multilayer assembly [7,8] offers an alternative means of combining molecular units on mesoporous metal oxide substrates [9,10]. In a simple, stepwise fashion, it has enabled the generation of chromophore-catalyst [11], sensitizer-annihilator [12], and multi-chromophore energy cascade assemblies [13–15]. It has also emerged as an effective means of influencing the rate, efficiency, and direction of interfacial electron transfer via the incorporation of electrochemically inert spacers [16–18] and electron donor/acceptor molecules [19–21]. Expanding upon this work, here we generate a multilayer composed of an **N3** dye, zinc(II) linking ion, and cobalt(II) (2,2′-bipyridine)$_2$ (2,2′-bipyridine-4,4′-dicarboxylic acid) (**Co**) as depicted in Fig. 1. The initial goal was to use the geometrically restricted proximity imposed by the bilayer to increase

---

* Corresponding author.
E-mail address: hanson@chem.fsu.edu (K. Hanson).

https://doi.org/10.1016/j.jpap.2021.100088
Received 28 June 2021; Received in revised form 22 October 2021; Accepted 16 November 2021

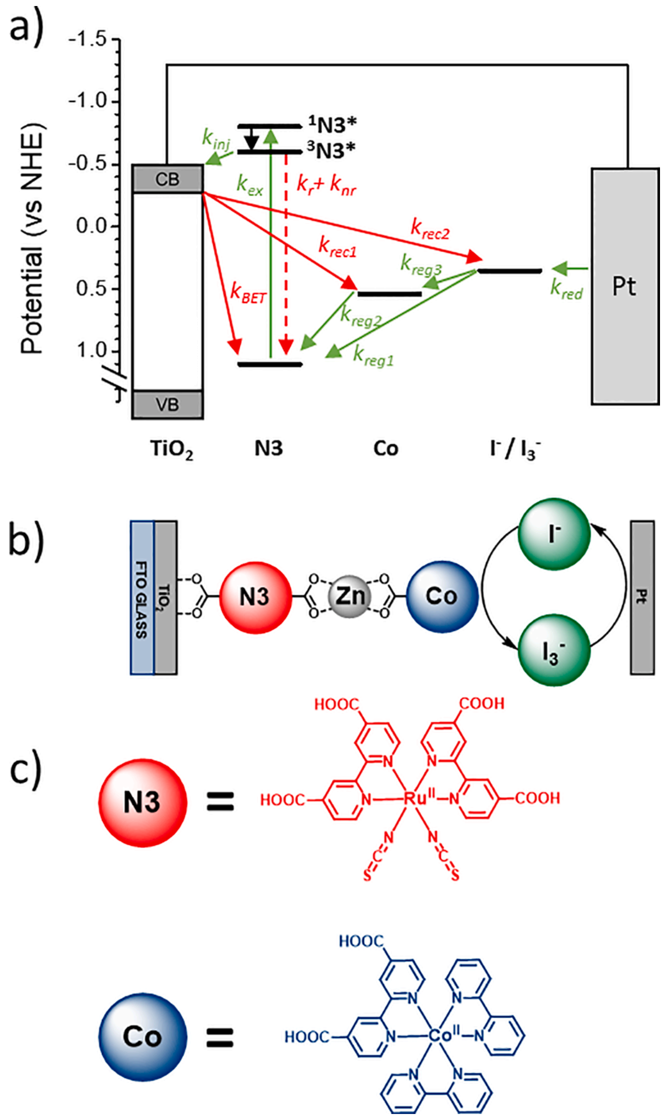

Fig. 1. a) Dynamic events and energetics (vs NHE) of TiO_2, **N3**, **Co**, and I^-/I_3^- with productive and non-productive processes in green and red respectively, b) schematic representation of bilayer, and c) molecular structure of **N3** and **Co**. (k_{ex} = excitation, k_r = radiative decay, k_{nr} = non-radiative decay, k_{inj} = electron injection, k_{BET} = back electron transfer, $k_{reg(n)}$ = regeneration, $k_{rec(n)}$ = recombination, k_{red} = mediator reduction).

the rate of **Co** to **N3**$^+$ electron transfer, inhibit/slow k_{BET} and k_{rec}, and increase the performance of a DSSC containing I^-/I_3^- redox mediator via an electron transfer cascade mechanism. However, through a combination of spectroscopic and device measurements, we demonstrate that despite **Co** to **N3**$^+$ electron transfer readily occurring in solution, their incorporation into the bilayer motif sufficiently restricts molecular motion such that electron transfer is hindered.

Experimental

Materials

Zinc perchlorate hexahydrate, cis-Bis(isothiocyanato)bis(2,2′-bipyridyl-4,4′-dicarboxylato)ruthenium(II) (**N3**), sodium hydroxide pellets, and acetonitrile were purchased from Sigma Aldrich and used without any further purification. Bis(2,2′-bipyridine)(2,2′-bipyridine-4,4′-dicarboxylic acid)cobalt(II) 2 Cl$^-$ (**Co**) was synthesized with modifications to literature procedure [22,23] with additional details provided in the supporting information. Non-FTO glass and fluorine-doped tin oxide (FTO)-coated glass (sheet resistance 15 Ω □$^{-1}$) was purchased from Hartford Glass Co. Melatonix film (1170−25) and Vac'n Fill syringes (65,209) were purchased from Solaronix. Micro glass cover slides (18 × 18 mm) were obtained from VWR. TiO_2 and ZrO_2 solgel pastes and films for spectroscopic measurements were prepared following previously reported procedures. [24,25] DSSCs measurements were performed using anodes prepared with TiO_2 paste purchased from Solaronix (002, 010). 1-Butyl-3-methylimidazolium iodide (BMII, Aldrich) and Iodine (I_2, Fisher Scientific) were purchased from providers in parentheses. ^{101}Ru, ^{66}Zn, and ^{59}Co ICP-MS standards were purchased from Inorganic Ventures at 1000 μg/mL and used with HPLC grade water purchased from Sigma Aldrich.

Sample preparation- cell fabrication

TiO_2 or ZrO_2 films for spectroscopic measurements were prepared by doctorblading the respective pastes onto a glass substrate using one layer of Scotch tape to control the thickness. The dried films were then sintered in an oven at 500 °C and 430 °C for TiO_2 and ZrO_2 with the heating and cooling cycle from previously published procedures [24, 25]. Device samples were made using nanocrystalline TiO_2 films (~5 μm thick), by screen printing Dyesol 18 NR-T TiO_2 paste with a screen printer (Dyenamo, DN—HM02). These films were subsequently sintered at 500 °C for 15 min. Molecules were then loaded as described in the next section. A small hole was drilled into the corner of a 2 × 2 cm glass slide (for spectroscopic samples) or 1.5 × 1 cm glass slide coated with Pt from dropcasting H_2PtCl_6 in ethanol (50 μL, 5 mM) and heat-drying at 400 °C for 20 min (device samples). The metal oxide glass slide and the cover slide (spectroscopic sample) or cathode (device sample) was then sealed using cut Melatonix film and heated to 150 °C for 7 s using a home-built pressure and heating plate [16]. Spectroscopic samples were transferred to a glovebox and injected with dry and oxygen-free acetonitrile using a Vac'n Fill syringe and the previously drilled hole was sealed with a piece of Melatonix and micro glass cover slide. Samples for DSSC measurements were similarly injected but with the iodide/-triiodide mixture (0.1 M BMII and 0.01 M I_2) in acetonitrile outside of the glovebox.

Dye loading

TiO_2 films were immersed in 400 μM **N3** in ethanol for 6 h, then rinsed with hexanes, and dried with a stream of air. For multilayer assemblies, the MO_2-**N3** films were then immersed in 500 μM solution of zinc perchlorate in ethanol for two hours, rinsed with hexanes, and dried with a stream of air. Finally, unless otherwise noted, samples were immersed in 300 μM **Co** in acetonitrile for three hours, rinsed with hexanes, and dried with a stream of air. The surface coverage for **N3** was calculated using the expression $\Gamma = (A(\lambda)/\varepsilon(\lambda))/1000$, where Γ is the surface coverage in mol cm^{-2}, A(λ) is the absorbance of the film, and ε(λ) is the solution extinction coefficient for **N3** which is 1.42×10^4 M^{-1} cm^{-1} at 538 nm in ethanol [26]. Surface coverage of **Co** was then calculated relative to **N3** based on the **N3:Co** ratios as determined by inductively coupled plasma mass spectrometry (*vida infra*). The **Co** adsorption isotherm (Fig. S3) was fit using $\Gamma = K_{ad}((\Gamma_{max} \times [Co])/(1 + \Gamma_{max} \times [Co]))$ to give the equilibrium adsorption constant (K_{ad}) and in accord with the Langmuir isotherm model [27].

Absorption spectroscopy

UV−visible spectra were recorded using an Agilent 8453 UV−visible photodiode array spectrophotometer by placing the dye-loaded TiO_2 slides perpendicular to the detection beam path.

Attenuated total reflectance infrared spectroscopy (ATR-IR)

ATR-IR spectra were recorded using a Bruker Alpha FTIR spectrometer (SiC Globar source, DTGS detector) with a Platinum ATR quickSnap sampling module (single-reflection diamond crystal).

Inductively coupled plasma mass spectrometry (ICP-MS)

TiO_2-**N3** and TiO_2-**N3**-Zn films were prepared following the procedure described above. Samples were then submerged in 300 μM, 150 μM, 75 μM, 25 μM, and 10 μM **Co** in MeCN for three hours. Assemblies were then desorbed from the surface using 3 mL of 0.1 M NaOH in HPLC grade water for two hours. ICP-MS data were recorded on Thermo Fisher Scientific iCAP RQ ICP-MS equipped with an ASX-280 autosampler (Teledyne, Cetak Technologies), and operated by the Qtegra software from Thermo Scientific. Measurements were acquired in standard mode at 1500 W plasma RF power. The nebulizer, auxiliary, and cool gas flow rates were 1.056, 0.8, and 14 L min^{-1}, respectively. Mass calibration was performed weekly using the iQAP Q calibration solution (Fisher Scientific) containing 7 elements in 2% HNO_3. Mass accuracy, sensitivity, detector cross calibration, and signal stability were optimized prior to each run using the iQAP Q/RQ tune solution (Fisher Scientific) containing 1.0 μg L^{-1} Ba, Bi, Ce, Co, In, Li, and U in 2% HNO_3, and 0.5% HCl. Calibration curves were obtained along with each run on the ICP-MS using the Co, Zn, and Ru standard from Inorganic Ventures. To prepare standard solutions for calibration, working solutions of Co, Zn, and Ru (1000 ppb) were obtained by diluting primary stock solutions with HPLC grade water and HNO_3 to achieve a final concentration of 2% HNO_3. Calibration standards of 0, 0.5, 1, 5, 10, and 25 ppb were obtained by dilution of working solutions with HPLC grade water and HNO_3 to achieve a final concertation of 2% HNO_3. Due to batch-to-batch film variability (i.e. thickness and total surface area), the absolute concentrations in ppb is only reported for one set of samples. However, the maximum loading ratio of Co and Zn relative to ^{101}Ru is the average calculated from three independent trials with bilayers prepared using a 300 μM **Co** loading solution.

Device characterization

Photocurrent density−voltage curves and electrochemical impedance spectroscopy measurements were performed as previously reported [28]. Details of these procedures are provided in the Supporting Information.

Transient absorption

Nanosecond (Edinburgh LP980 and Continuum Surelite with Horizon OPO) and ultrafast (Helios FIRE and Vitara-S Coherent with OPerA Solo OPA) transient absorption measurements were performed on commercially available spectrometers and lasers with details provided in the SI. Kinetic decays were fit using a biexponential function (Eq. (1)), and reported as the weighted average lifetime/rate constant (Eq. (2)):

$$y = A_1 e^{-k1x} + A_2 e^{-k2x} + y_0 \tag{1}$$

$$\tau_i = \frac{1}{k_i}; \langle\tau\rangle = \sum A_i \tau_i^2 \Big/ \sum A_i \tau_i \tag{2}$$

Results and discussion

I. Surface loading

TiO_2-**N3** films were prepared by submerging the mesoporous TiO_2 in a 400 μM **N3** in ethanol for 6 h with dye loading monitored using UV–Vis spectroscopy (Fig. S1). In accord with literature [29], these conditions enabled maximum, near full monolayer loading of **N3** on TiO_2 ($\Gamma = 5.7 \times 10^{-8}$ mol•cm^{-2}). For bilayer film preparation, TiO_2-**N3** was then immersed for two hours in an ethanol solution containing 500 μM $Zn(ClO_4)_2$. Zn^{2+} coordination to the non-surface bound COOH groups of **N3** (TiO_2-**N3**-Zn) was indicated by the disappearance of C—O stretches 1100 cm^{-1} and increased intensity of COO^- stretches (1540 and 1600 cm^{-1}) in the ATR-IR spectra (Fig. 2) [30]. It is worth noting that initial attempts to load the linking ion using $Zn(OAc)_2$ resulted in notable desorption of **N3** from the surface. Presumably, the acetate either competitively adsorbs to the surface or it makes the solution sufficiently basic that **N3** binding is no longer favorable [31]. Regardless of the cause, no such desorption was observed when using the perchlorate counter ion.

Finally, the bilayer film was prepared by submerging TiO_2-**N3**-Zn in an acetonitrile solution containing 300 μM of **Co**. Typically, multilayer loading is monitored using UV–Vis spectroscopy [32]. However, the π-π* transition of **Co** at ~300 nm [33] overlaps with the spectral features of both **N3** and TiO_2 (Fig. S2) making quantification by spectral deconvolution impractical. However, the presence of **Co** in the bilayer was confirmed by ATR-IR spectroscopy (Fig. 2). In comparison to TiO_2-**N3**-Zn, upon **Co** loading there is a dramatic increase in symmetric (1600 cm^{-1}) and asymmetric (1540 cm^{-1}) COO^- stretches and C—O stretch at 1100 cm^{-1} that are consistent with the COOH groups of **Co** [30]. Unfortunately, direct quantification of **Co** loading by ATR-IR was impeded by the pressure/surface roughness dependent nature of the signal amplitude.

To obtain a comparative estimate of surface coverage, inductively coupled plasma mass spectrometry (ICP-MS) was used to quantify the relative ratios of **N3**, Zn, and **Co** in the bilayer films. Following the loading procedure described above, the molecules were desorbed from the surface using a 0.1 M NaOH aqueous solution. These solutions were then diluted to ppb concentrations in nitric acid and the concentrations of ^{101}Ru, ^{66}Zn, and ^{59}Co were determined using calibration curves generated with ICP-MS standards and the results are summarized in Table 1 and Fig. S3.

As can be seen in Table 1, the TiO_2-**N3**-Zn film has as large as a 1:1.5 ratio of **N3**:Zn. Given that two of the four COOH groups of **N3** are not bound to the surface [34], this suggests that half of the **N3** molecules only have one Zn bound or alternatively, there may be COO-Zn-OOC bridges between adjacent **N3** molecules. Regardless of the configuration, the TiO_2-**N3**-Zn films contain at least one Zn per **N3** molecule. Equally notable is that the Zn loading procedure does not decrease the concentration of **N3**.

While the absolute concentration of the species varied due to batch-to-batch sample variation (i.e. thickness and total surface area), the ratio of ^{101}Ru:^{59}Co ratio under 300 μM **Co** loading was found to be consistently at 10:0.9 ± 0.2 across three independent samples with the error

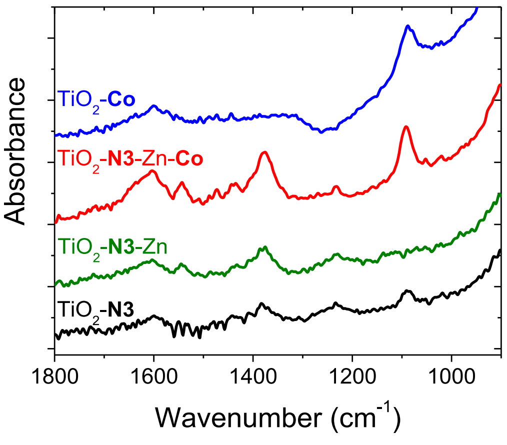

Fig. 2. ATR-IR spectra of TiO_2-**N3** (black), TiO_2-**N3**-Zn (green), TiO_2-**N3**-Zn-**Co** (red), and TiO_2-**Co** (blue).

Table 1

Concentrations (in ppb) of ^{101}Ru, ^{66}Zn, and ^{59}Co determined from ICP-MS of desorbed films of TiO_2-**N3**, TiO_2-**N3**-Zn and TiO_2-**N3**-Zn-**Co** bilayers with varying concentrations of the **Co** loading solutions.[a]

	TiO_2-**N3**	TiO_2-**N3**-Zn	TiO_2-**N3**-Zn-**Co** [**Co**] of the loading solution				
			10 μM	25 μM	75 μM	150 μM	300 μM
^{59}Co	0.004	0.003	0.293	0.833	0.694	1.007	1.031
^{66}Zn	0.097	21.266	17.319	18.702	19.388	9.597	12.941
^{101}Ru	14.045	14.798	14.711	14.871	14.766	13.681	12.752

[a] Absolute concentrations are for one representative sample set.

being the standard deviation of those trials. The loading of **Co** on TiO_2-**N3**-Zn also exhibits isotherm behavior with a K_{ad} of 4.7 × $10^6\ M^{-1}$ and has a surface coverage of ~6 × 10^{-9} mol•cm^{-2} (calculated relative to **N3**, $\Gamma_{N3} = 5.7 \times 10^{-8}$ mol•cm^{-2}) when loaded from >150 μM **Co** solution (Fig. S3). Consequently, all subsequent MO_2-**N3**-Zn-**Co** bilayer films were prepared using a 300 μM **Co** solution to ensure maximum surface loadings of **Co**. Interestingly, this maximum loading ratio of ~10:1, **N3:Co**, is lower than other previously reported bilayers which achieve as high as a 3:1 first to second layer ratio [32]. In line with our recent report, it is possible that the relatively large size of **Co** and the limited pore size of the metal oxide may hinder full bilayer formation in the film [35]. Alternatively, the octahedral geometry of **N3** most likely results in geometric hinderances for the second layer loading. More specifically, with two COOH groups of **N3** bound to the surface, the two remaining COOH groups are largely orthogonal to the surface normal [36] effectively hindering access for Zn^{2+} and **Co** binding. This is contrast to our previously reported first layer molecules with diametrically opposed surface binding and metal-ion linking groups that are expected to be more accessible resulting in a much higher second layer loading[52].

In summary, the above results indicate that the TiO_2-**N3**-Zn-**Co** bilayer can be formed and that the surface coverage and relative ratio of **Co** can be controlled by varying the concentration of the loading solution. Equally, if not more important, we have demonstrated that ICP-MS is an effective tool for quantifying the relative surface loading of UV–Vis spectroscopically "silent" species like Zn^{2+} and **Co** in metal ion linked multilayers.

II. Dye-sensitized solar cells

DSSCs were assembled in a sandwich cell architecture following previously published procedures [28,37] with TiO_2-**N3**, TiO_2-**N3**-Zn, or TiO_2-**N3**-Zn-**Co** as the photoanode, platinum-coated FTO glass as the cathode, and iodide/triiodide in MeCN as the electrolyte solution. The energetics and dynamic events for the DSSCs are depicted in Fig. 1. Note that the I^-/I_3^- redox mediator was selected as opposed to the decarboxylated **Co** analogue, $Co(bpy)_3^{2+/3+}$[38], to ensure sufficient driving force for k_{reg3}.

Photocurrent density–voltage ($J-V$) curves were measured, and the results are shown in Fig. 3 and Fig. S4 and the performance metrics are summarized in Table 2. Results are reported under both AM1.5 irradiation and AM1.5 irradiation passed through a 375 nm long pass filter (AM1.5 + 375 LP), with the latter being used to prevent any unintended consequences of direct excitation of **Co** in the bilayer film. As can be seen in Table 2, the trends in performance are similar with and without the filter, suggesting that direct excitation of **Co** does not impact the performance outcome. Consequently, we will focus our discussion on the non-filtered data.

Of the three devices, the parent TiO_2-**N3** exhibited the highest overall photocurrent density (J_{SC}), fill factor (FF), and power conversion efficiency (PCE). In agreement with our previous observations, [28,37] the coordination of zinc to **N3** (TiO_2-**N3**-Zn) decreases the J_{SC} from 2.10 to 1.62 mA/cm^2 but increases the V_{OC} from 590 to 630 mV. The decrease in J_{SC} and increase in V_{OC} are attributed to the additional steric bulk of the Zn ion decreasing regeneration rate of **N3**$^+$ by the mediator and slowing recombination between the electron in TiO_2 and the redox mediator. Interestingly, the devices containing the TiO_2-**N3**-Zn-**Co** films gave the lowest performance in every device metric. This outcome is in direct contrast with the increase in J_{SC} and V_{OC} one would expect if the cobalt were serving to increase the rate of regeneration and slow recombination.

To gain insights into the dynamic events in the device, electrochemical impedance spectroscopy (EIS) was performed under AM1.5 irradiance and the resulting Nyquist plot is shown in Fig. 4. In a usual Nyquist plot for a DSSC, three semi-circles can be observed [39], but the mid-frequency arc is typically the most prominent feature and is attributed to the resistance to recombination (R_{recomb}) at the TiO_2-dye-electrolyte interface. As can be seen in Fig. 4, for all three devices

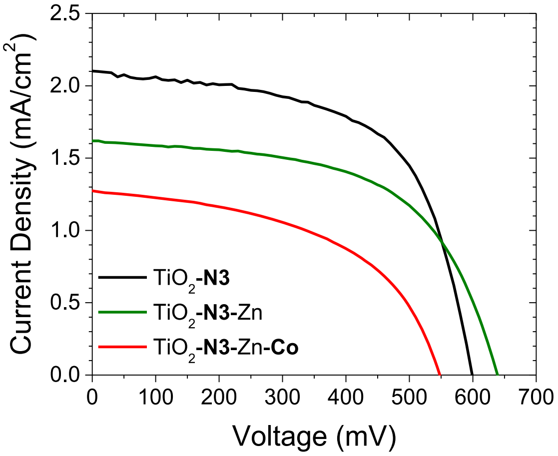

Fig. 3. Photocurrent density–voltage curves for DSSCs with photoanodes composed of TiO_2-**N3**, TiO_2-**N3**-Zn, and TiO_2-**N3**-Zn-**Co** with I^-/I_3^- redox mediator under AM 1.5 irradiation (100 mW/cm^2).

Table 2

Performance characteristics of DSSCs containing TiO_2-**N3**, TiO_2-**N3**-Zn, and TiO_2-**N3**-Zn-**Co** photoanodes with I^-/I_3^- redox mediator in MeCN.[a]

Anode	Light Source	J_{SC} (mA/cm^2)	V_{OC} (mV)	FF (%)	PCE (%)
TiO_2-**N3**	AM1.5	2.10 ± 0.15	590 ± 5	61 ± 4.0	0.76 ± 0.05
	AM1.5 + 375 LP	1.63 ± 0.09	590 ± 9	62 ± 2.3	0.59 ± 0.03
TiO_2-**N3**-Zn	AM 1.5	1.62 ± 0.05	631 ± 20	59 ± 1.3	0.60 ± 0.05
	AM1.5 + 375 LP	1.28 ± 0.10	625 ± 27	60 ± 0.8	0.48 ± 0.05
TiO_2-**N3**-Zn-**Co**	AM 1.5	1.27 ± 0.28	546 ± 22	51 ± 2.6	0.35 ± 0.08
	AM1.5 + 375 LP	1.01 ± 0.22	540 ± 22	52 ± 1.8	0.28 ± 0.07

[a] All data are the average value from the measurement of three separate DSSCs and the error (±) are the standard deviation of those measurements.

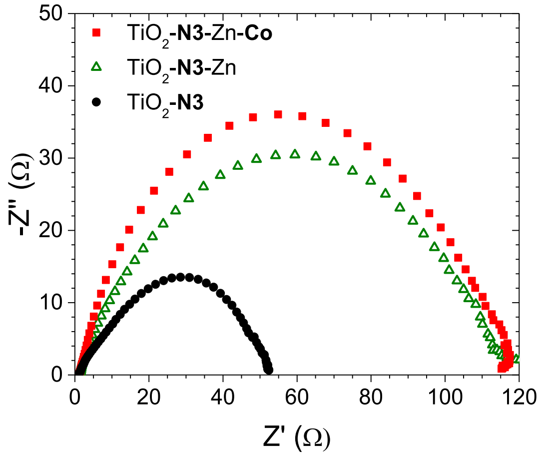

Fig. 4. Nyquist plots obtained from EIS for TiO_2-**N3**, TiO_2-**N3**-Zn, and TiO_2-**N3**-Zn-**Co** devices at open-circuit voltage under AM 1.5 irradiation (100 mW/cm^2).

the middle arc is the only readily discernible feature with R_{recomb} increasing in the order of TiO_2-**N3** < TiO_2-**N3**-Zn < TiO_2-**N3**-Zn-**Co**. Presumably, the addition of Zn and **Co** inhibit recombination losses, relative to TiO_2-**N3**, due to additional steric bulk between $TiO_2(e^-)$ and the oxidized mediator in solution. If this were the only contributing factor, one would anticipate the highest V_{OC} for the TiO_2-**N3**-Zn-**Co** device. But the lowest V_{OC} for TiO_2-**N3**-Zn-**Co** indicates that any gains in inhibiting recombination are offset by decreases in the total number of electrons in TiO_2 (i.e. lower injection yield, slower regeneration, etc.).

III. Transient absorption

Transient Absorption Spectroscopy (TAS) was used to gain additional insights into the excited state dynamics of TiO_2-**N3**, TiO_2-**N3**-Zn, and TiO_2-**N3**-Zn-**Co** films. TiO_2-**N3** and TiO_2-**N3**-Zn films exhibited a spectral shift but similar kinetics in the absence of I^-/I_3^- (Fig. S5 and S6) so only **N3, N3**-Zn-**Co** films will be discussed below.

To investigate the possibility of excited state quenching of **N3** by **Co** [37], we measured the excited state spectral evolution for ZrO_2-**N3** and ZrO_2-**N3**-Zn-**Co**. Mesoporous ZrO_2 was chosen as the substrate for these measurements because its nearly 1 V more negative conduction band (−1.4 V vs NHE) compared to TiO_2 (−0.5 V vs NHE) [40] inhibits excited state electron transfer from **N3** to the metal oxide. As can be seen in Fig. S7, the decay kinetics are nearly identical in both films with no new spectral features observed. This indicates that if there is a possible quenching mechanism in the **N3**-Zn-**Co** bilayer, it is slower than the intrinsic excited state decay of **N3** on ZrO_2 (~25 ns) [40,41].

On TiO_2, where electron injection can occur, following 480 nm excitation, both TiO_2-**N3** and TiO_2-**N3**-Zn-**Co** exhibit characteristic features for the ground state bleach of N3 at 550 nm, the triplet excited state of **N3** at 690 nm, as well as **N3** cation at 750 nm (Fig. 5) [42]. This is consistent with previous reports describing sub-picosecond electron injection dynamics from **N3*** to TiO_2 [43]. The similarity in the early time kinetics TiO_2-**N3** and TiO_2-**N3**-Zn-**Co** indicates that neither **Co** nor the bilayer architecture has any notable impact on the electron injection event (TiO_2-**N3*** → $TiO_2(e^-)$-$\mathbf{N3}^+$).

The fate of the **N3** cation in TiO_2-**N3** and TiO_2-**N3**-Zn-**Co** films was then monitored on longer timescales using nano- to microsecond TAS and the results are shown in Fig. 6 and Fig. S8. In the TA spectra of both films, we observe the ground state bleach at ~550 nm and a broad positive going peak centered at ~750 nm that are consistent with the presence of $\mathbf{N3}^+$ which returns to baseline (i.e. **N3**) in less than 20 μs (Fig. S8). In the absence of an electron donating redox mediator in solution, back electron transfer is the primary mechanism for the reappearance of ground state **N3** in TiO_2-**N3** (Eq. (3)). [4] For the TiO_2-**N3**-Zn-**Co** film, in addition to the back electron transfer mechanism (Eq. (4)), **Co** could act as an electron donor for the regeneration of **N3** (Eq. (5)) resulting in the $TiO_2(e^-)$-**N3**-Zn-$\mathbf{Co}^+$ charge separated species.

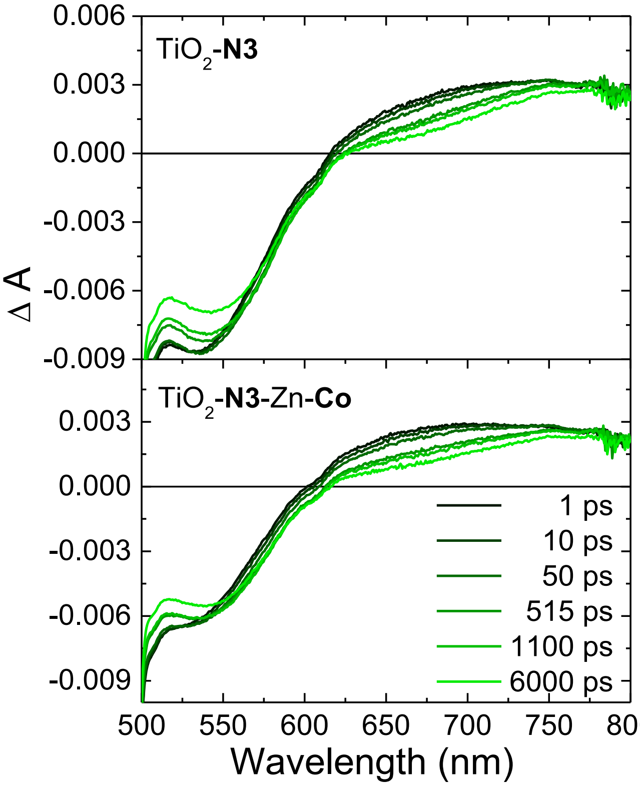

Fig. 5. Transient absorption spectra for TiO_2-**N3** (top) and TiO_2-**N3**-Zn-**Co** (bottom) in MeCN (λ_{ex} = 480 nm) from 1 ps to 6000 ps.

$$TiO_2(e^-) - \mathbf{N3}^+ \rightarrow TiO_2 - \mathbf{N3} \quad (3)$$

$$TiO_2(e^-) - \mathbf{N3}^+ - Zn - \mathbf{Co} \rightarrow TiO_2 - \mathbf{N3} - Zn - \mathbf{Co} \quad (4)$$

$$TiO_2(e^-) - \mathbf{N3}^+ - Zn - \mathbf{Co} \rightarrow TiO_2(e^-) - \mathbf{N3} - Zn - \mathbf{Co}^+ \quad (5)$$

The lack of new spectral features (Fig. S8) and the nearly identical $\mathbf{N3}^+$ decay kinetics at 750 nm Fig. 6a) for both TiO_2**N3** ($\tau_{N3}{}^+$ = 5.2 ± 0.4 μs) and TiO_2-**N3**-Zn-**Co** ($\tau_{N3}{}^+$ = 4.3 ± 0.3 μs) suggests that back electron transfer (Eqs. (3) and ((4) is the primary recombination mechanism in both films. Consequently, if **Co** to $\mathbf{N3}^+$ electron transfer is occurring in the film, the high-end estimate of the rate is on the order of $4.0 \times 10^4\ s^{-1}$. It is important to note that due to the low **N3:Co** ratio (10:1), cross-surface cation migration from **N3** to a **N3**-Zn-**Co** dyad could also contribute to slowed **Co** to $\mathbf{N3}^+$ electron transfer. Anisotropy measurements and Monte Carlo simulations on related ruthenium polypyridyl complexes indicate that ~60 lateral hole-hopping events can occur prior to recombination [44]. Consequently, even at a 10:1 ratio, we anticipate that cation migration to a **N3**-Zn-**Co** dyad can readily occur prior to recombination and that regeneration is limited by **Co** to $\mathbf{N3}^+$ electron transfer.

We also performed the same measurement but under device relevant conditions (i.e. with 0.1 M BMII and 0.01 M I_2 in MeCN) and the results are shown in Fig. 6b. For the TiO_2-**N3** , the addition of I^- decreases the lifetime from 5.2 μs to 3.1 μs due to electron transfer from I^- to $\mathbf{N3}^+$ (k_{reg1} in Fig. 1). k_{reg1} for TiO_2**N3** under these conditions is calculated to be $1.3 \times 10^5\ s^{-1}$ using Eq. (6) where $\tau_{N3+(I-)}$ and $\tau_{N3}+$ are the $\mathbf{N3}^+$ lifetime with and without the redox mediator in solution.

$$k_{reg1} = \frac{1}{\tau_{N3^+(I-)}} - \frac{1}{\tau_{N3^+}} \quad (6)$$

There is a subtle but reproducibly slower k_{reg1} for TiO_2-**N3**-Zn-**Co**

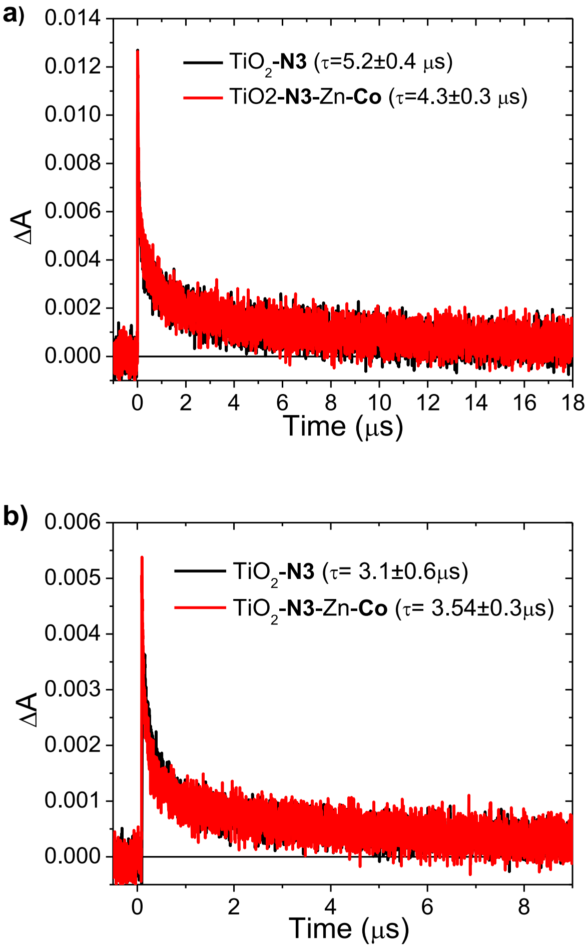

Fig. 6. Transient absorption kinetics traces at 750 nm for TiO$_2$-**N3** (black) and TiO$_2$-**N3**-Zn-**Co** (red) in MeCN ($\lambda_{ex} = 480$ nm) without (a) and with (b) 0.1 M BMII and 0.01 M I$_2$. The reported lifetimes are the average of three independent samples with the error being the standard deviation.

(0.5×10^5 s^{-1}). Presumably, although **Co** has minimal direct involvement in interlayer electron transfer, it serves as at least some steric bulk that inhibits contact between **N3**$^+$ and I$^-$. But, the impact of that steric blocking is likely minimized due to the low surface coverage and fast cross surface cation migration which is on the order of 10^8–10^{11} s^{-1} for dyes on TiO$_2$ [10]. In a similar vein, although electrostatics between Zn^{2+} and *I*$^-$ is expected to increase regeneration rates, previous results indicated that any gains due to electrostatics are offset by the steric hinderance of Zn^{2+} between **N3**$^+$ and I$^-$. [28] This steric bulk may also be responsible for slowing TiO$_2$(e$^-$) to I$_3$$^-$ recombination and the increased recombination resistance for TiO$_2$-**N3**-Zn-**Co** seen in EIS measurements (Fig. 4).

IV. Interlayer electron transfer

Collectively, and contrary to our initial goal, the above results indicate that **Co** to **N3**$^+$ electron transfer is a slow/negligible process in the metal ion linked multilayer film. This lack of electron transfer is a bit surprising given that related cobalt polypyridyl complexes are well known as regenerative electron donors in DSSCs. [45–47] As described by Marcus theory [48,49], electron transfer between an electron donor and acceptor is primarily dictated by the reorganization energy (λ), Gibbs free energy change (ΔG^o), and donor-acceptor electronic coupling (H$_{AB}$). Given similar energetics and structure to known cobalt polypyridyl mediators [50,51] we do not expect λ and ΔG^o to hinder electron transfer from **Co**. To further probe these energetic requirements, we performed transient absorption on TiO$_2$-**N3** with and without 0.1 M **Co** in solution (i.e. without the Zn(II) linking ion) and the results can be seen in Fig. 7. The **N3**$^+$ lifetime decreases from 5.2 μs to 2.7 μs in the presence of **Co** giving a k_{reg1} of 1.8×10^5 s^{-1} (from Eq. (6) but with/without **Co**) which is comparable to that of I$^-$ (1.3×10^5 s^{-1}). Consequently, there is no intrinsic energetic barrier to **Co** to **N3**$^+$ electron transfer.

The interlayer electron transfer rate (k_{reg2}) is proportional to the square of the electronic coupling element (H$_{DA}$) which is dependent on the distance, orientation, and intervening medium between the electron donor and acceptor [48]. To gain some insights into the bilayer structure, we used semi-empirical, molecular mechanics simulations (PM3, Spartan) to determine the equilibrium geometry of **N3**-Zn-**Co**. From this structure we obtain a center-to-center distance of ~18 Å between **N3** and **Co** in the bilayer (Fig. 8) [52]. Previous DFT calculations estimate center-to-center distances as low as 8 Å when **N3** is bound to a surface and unsubstituted cobalt polypyridal complexes are free to diffuse in solution [51]. Here, with the addition COOH groups, we assume a diffusional distance of ~10 Å. It is likely that the two-fold increase in center-to-center distance between **N3** and **Co** dramatically slows the electron transfer rate (k_{eT}) in the bilayer relative to solution.

The donor-acceptor coupling (H$_{DA}$), and consequently k_{eT} exhibits a well know exponential distance dependence as described by Eq. (7) [53], where β is the attenuation coefficient, R_o is the van der Waals distance between donor and acceptor, R_{DA} is the donor acceptor separation of interest, and k^o_{eT} is the electron transfer rate constant at close contact.

$$k_{eT} = k^o_{eT}\exp(-\beta(R_{DA} - R_o)) \tag{7}$$

Assuming a k^o_{eT} of 4×10^5 s^{-1} [50], and a high-end estimate of R_o of 10 Å we have calculated the relationship between k_{eT} and R_{DA} with β values ranging from 2.5 Å^{-1} (in vacuum) to 0.1 Å^{-1} (molecular wires) and the results can be seen in Fig. 9.

From the experimental **Co** to **N3**$^+$ electron transfer rate of 4.0×10^4 s^{-1}, an assumed center-to-center distance ranging from 15 to 18 Å (i.e. accounting for possible flexibility in the linkage and **Co** orientation), and the data in Fig. 9, we can estimate a β value from 0.25 to 0.5 Å^{-1} for the metal ion linked multilayer. This range of β value suggests that the Py-COO-Zn-COO-Py linking motif is similarly "conductive" to a phenyl bridge system (β = 0.2–0.5 *Å*$^{-1}$) and more than an sp^3 carbon chain (β = 1 Å^{-1}), for example [54,55]. The role of the metal linking ion in dictating the β value is not known at this time but may provide an

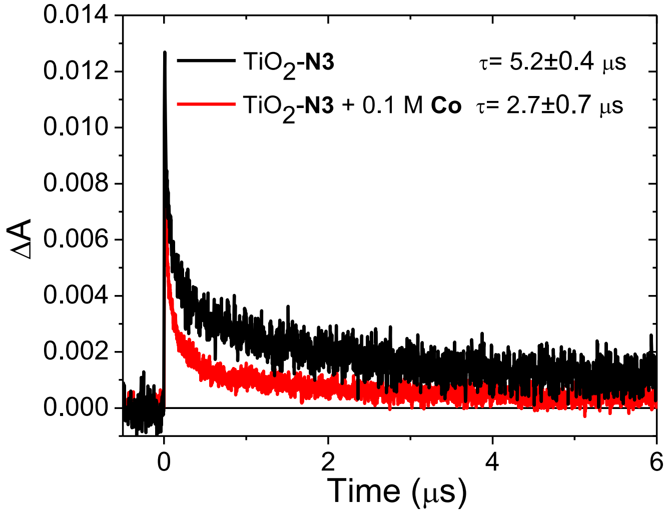

Fig. 7. Transient absorption kinetics traces at 750 nm for TiO$_2$-**N3** in MeCN ($\lambda_{ex} = 480$ nm) without (black) and with 0.1 M **Co** (red). The reported lifetimes are the average of three independent samples with the error being the standard deviation.

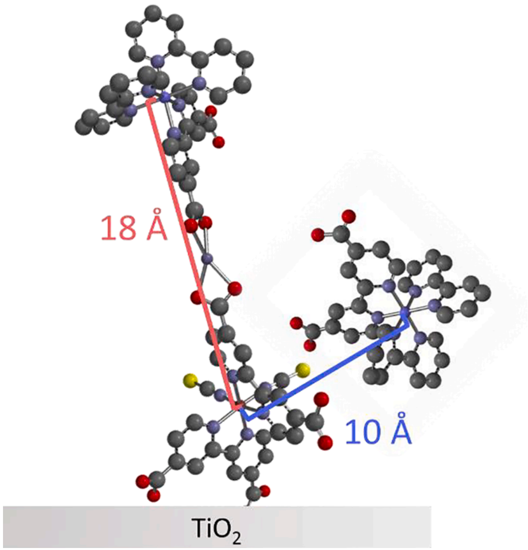

Fig. 8. Approximate center-to-center distances between **N3** and **Co** in TiO_2-**N3**-Zn-**Co** (red) and with **Co** in solution (blue).

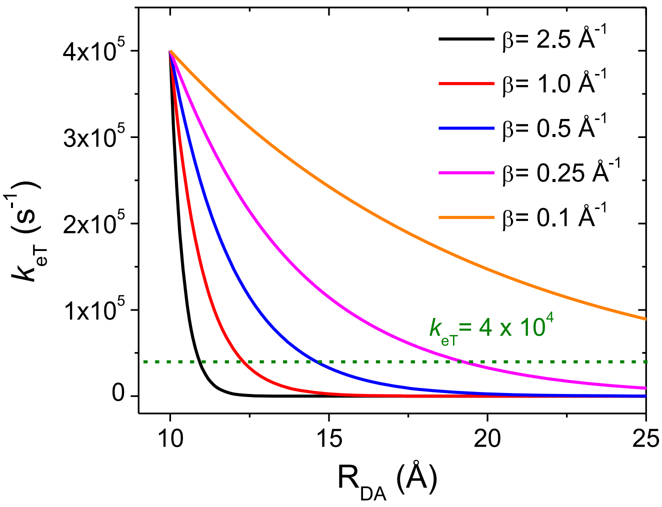

Fig. 9. Calculated relationship between k_{eT} and R_{DA} with various β values ranging from 2.5 $Å^{-1}$ to 0.1 $Å^{-1}$ assuming a k^o_{eT} of 4×10^5 s^{-1}, and an R_o of 10 Å. The green dashed line represents the observed k_{eT} in the bilayer.

additional, tunable variable for influencing interlayer electron transfer [56–58]. Alternatively, we cannot currently rule out electron transfer from **Co** to an adjacent **N3** molecule (i.e. an **N3** that is not in the **N3**-Zn-**Co** bilayer) which could reduce the center-to-center distance and give an artificially low attenuation coefficient.

Conclusion

Here we report the spectroscopic and dye-sensitized device characterization of a **N3**-Zn linking ion-**Co** electron donor, multilayer assembly on mesoporous TiO_2. The film formation and loading ratios were determined using a combination of UV–Vis, ATR-IR, and ICP-MS. The latter is particularly notable in that we have demonstrated that ICP-MS can be used as a tool for quantification of spectroscopically obscured molecules in metal ion linked multilayers.

Surprisingly, incorporating the **Co** electron donor into the multilayer decreases the DSSC response in nearly every performance metric (i.e. J_{SC}, V_{OC}, FF, PCE). EIS and J-V measurements suggest that while the cobalt complex helps to inhibit recombination, those gains are more than offset by a decrease in the photocurrent of the film. Initially we anticipated that **Co** would serve as an electron donor to the oxidized dye, but transient absorption measurements indicate that **Co** is largely inert in the bilayer with both excited state quenching and **Co** to **N3**$^+$ electron transfer being slower than the excited state decay and recombination, respectively. But the steric bulk of **Co** may serve to hinder both **N3**$^+$ regeneration and $TiO_2(e^-)$ to I_3^- recombination which resulted in a net decrease in device performance.

While **Co** to **N3**$^+$ electron transfer readily occurs in solution, the geometric restriction imposed by the multilayer architecture effectively slows interlayer electron transfer. The large center-to-center distance is sufficient to slow interlayer electron transfer to the point of not being competitive with intrinsic excited state decay, electron injection, and recombination dynamics at the dye- semiconductor interface. Consequently, this particular combination of molecules is not useful in DSSCs, but these insights could be used to guide the design of new multilayers with smaller spatial separation and increased electron transfer rates. Alternatively, this multilayer architecture may be useful in other applications where electron transfer is not desired but say communication of spin and/or magnetic moment is needed.

Declaration of Competing Interest

The authors declare that they have no known competing financial interests or personal relationships that could have appeared to influence the work reported in this paper.

Acknowledgments

Spectroscopic measurements were partially supported by the National Science Foundation under Grant No. DMR-1752782. Structural characterization of the bilayer and device measurements were supported by the Army Research Office under Grant No. W911NF-19–1–0357. Ultrafast transient absorption measurements were performed on a spectrometer supported by the National Science Foundation under Grant No. CHE-1919633. A portion of these measurements were conducted in the FSU Department of Chemistry and Biochemistry's Mass Spec (FSU075000-MASS) and Materials Characterization (FSU075000-MAC) Laboratories.

Supplementary materials

Supplementary material associated with this article can be found, in the online version, at doi:10.1016/j.jpap.2021.100088.

References

[1] A. Hagfeldt, G. Boschloo, L. Sun, L. Kloo, H. Pettersson, Dye-sensitized solar cells, Chem. Rev. 110 (11) (2010) 6595–6663, https://doi.org/10.1021/cr900356p.

[2] M.K. Brennaman, R.J. Dillon, L. Alibabaei, M.K. Gish, C.J. Dares, D.L. Ashford, R. L. House, G.J. Meyer, J.M. Papanikolas, T.J. Meyer, Finding the way to solar fuels with dye-sensitized photoelectrosynthesis cells, J. Am. Chem. Soc. 138 (40) (2016) 13085–13102, https://doi.org/10.1021/jacs.6b06466.

[3] J.R. Swierk, T.E. Mallouk, Design and development of photoanodes for water-splitting dye-sensitized photoelectrochemical cells, Chem. Soc. Rev. 42 (6) (2013) 2357–2387, https://doi.org/10.1039/C2CS35246J.

[4] S. Ardo, G.J. Meyer, Photodriven heterogeneous charge transfer with transition-metal compounds anchored to TiO_2 semiconductor surfaces, Chem. Soc. Rev. 38 (1) (2009) 115–164, https://doi.org/10.1039/B804321N.

[5] W. Xu, B. Peng, J. Chen, M. Liang, F. Cai, New triphenylamine-based dyes for dye-sensitized solar cells, J. Phys. Chem. C 112 (3) (2008) 874–880, https://doi.org/10.1021/jp076992d.

[6] B. Pashaei, H. Shahroosvand, M. Graetzel, M.K. Nazeeruddin, Influence of ancillary ligands in dye-sensitized solar cells, Chem. Rev. 116 (16) (2016) 9485–9564, https://doi.org/10.1021/acs.chemrev.5b00621.

[7] D. Rong, H.G. Hong, Y.I. Kim, J.S. Krueger, J.E. Mayer, T.E. Mallouk, Electrochemistry and photoelectrochemistry of transition metal complexes in well-ordered surface layers, Coord. Chem. Rev. 97 (1990) 237–248, https://doi.org/10.1016/0010-8545(90)80092-8.

[8] H. Lee, L.J. Kepley, H.G. Hong, S. Akhter, T.E. Mallouk, Adsorption of ordered zirconium phosphonate multilayer films on silicon and gold surfaces, J. Phys. Chem. 92 (9) (1988) 2597–2601, https://doi.org/10.1021/j100320a040.

[9] K. Hanson, D.A. Torelli, A.K. Vannucci, M.K. Brennaman, H. Luo, L. Alibabaei, W. Song, D.L. Ashford, M.R. Norris, C.R.K. Glasson, J.J. Concepcion, T.J. Meyer, Self-assembled bilayer films of ruthenium(ii)/polypyridyl complexes through layer-by-layer deposition on nanostructured metal oxides, Angew. Chem. Int. Ed. 51 (2012) 12782–12785, https://doi.org/10.1002/anie.201206882.

[10] J.C. Wang, S.P. Hill, T. Dilbeck, O.O. Ogunsolu, T. Banerjee, K. Hanson, Multimolecular assemblies on high surface area metal oxides and their role in interfacial energy and electron transfer, Chem. Soc. Rev. 47 (1) (2018) 104–148, https://doi.org/10.1039/C7CS00565B.

[11] D.L. Ashford, M.K. Gish, A.K. Vannucci, M.K. Brennaman, J.L. Templeton, J. M. Papanikolas, T.J. Meyer, Molecular chromophore-catalyst assemblies for solar fuel applications, Chem. Rev. 115 (23) (2015) 13006–13049, https://doi.org/10.1021/acs.chemrev.5b00229.

[12] T. Dilbeck, K. Hanson, Molecular photon upconversion solar cells using multilayer assemblies: progress and prospects, J. Phys. Chem. Lett. 9 (19) (2018) 5810–5821, https://doi.org/10.1021/acs.jpclett.8b02635.

[13] O.O. Ogunsolu, I.A. Murphy, J.C. Wang, A. Das, K. Hanson, Energy and electron transfer cascade in self-assembled bilayer dye-sensitized solar cells, ACS Appl. Mater. Interfaces 8 (42) (2016) 28633–28640, https://doi.org/10.1021/acsami.6b09955.

[14] Y. Zhou, C. Ruchlin, A.J. Robb, K. Hanson, Singlet sensitization-enhanced upconversion solar cells via self-assembled trilayers, ACS Energy Lett. 4 (6) (2019) 1458–1463, https://doi.org/10.1021/acsenergylett.9b00870.

[15] T. Dilbeck, S.P. Hill, K. Hanson, Harnessing molecular photon upconversion at sub-solar irradiance using dual sensitized self-assembled trilayers, J. Mater. Chem. A 5 (23) (2017) 11652–11660, https://doi.org/10.1039/C7TA00317J.

[16] O.O. Ogunsolu, J.C. Wang, K. Hanson, Inhibiting interfacial recombination events in dye-sensitized solar cells using self-assembled bilayers, ACS Appl. Mater. Interfaces 7 (50) (2015) 27730–27734, https://doi.org/10.1021/acsami.5b08581.

[17] J.C. Wang, I.A. Murphy, K. Hanson, Modulating electron transfer dynamics at dye–semiconductor interfaces via self-assembled bilayers, J. Phys. Chem. C 119 (7) (2015) 3502–3508, https://doi.org/10.1021/jp5116367.

[18] R.E. Bangle, J. Schneider, D.T. Conroy, B.M. Aramburu-Trošelj, G.J. Meyer, Kinetic evidence that the solvent barrier for electron transfer is absent in the electric double layer, J. Am. Chem. Soc. 142 (35) (2020) 14940–14946, https://doi.org/10.1021/jacs.0c05226.

[19] B.H. Farnum, K.R. Wee, T.J. Meyer, Self-assembled molecular P/N junctions for applications in dye-sensitized solar energy conversion, Nat. Chem. 8 (9) (2016) 845–852, https://doi.org/10.1038/nchem.2536.

[20] B. Shan, S. Vanka, T.T. Li, L. Troian-Gautier, M.K. Brennaman, Z. Mi, T.J. Meyer, Binary molecular-semiconductor p-n junctions for photoelectrocatalytic CO_2 reduction, Nat. Energy 4 (4) (2019) 290–299, https://doi.org/10.1038/s41560-019-0345-y.

[21] R.N. Sampaio, L. Troian-Gautier, G.J. Meyer, A charge-separated state that lives for almost a second at a conductive metal oxide interface, Angew. Chem. Int. Ed. 57 (47) (2018) 15390–15394, https://doi.org/10.1002/anie.201807627.

[22] K. Arun Kumar, M. Amuthaselvi, A Dayalan, Cis-Bis(2,2′-bipyridine-κ^2*N,N'*) dichloridocobalt (II) trihydrate, Acta Cryst. E67 (2011) m468, https://doi.org/10.1107/S1600536811009251.

[23] R.J. Hue, R. Vatassery, K.R. Mann, W.L. Gladfelter, Zinc oxide nanocrystal quenching of emission from electron-rich ruthenium-bipyridine complexes, Dalton Trans. 44 (10) (2015) 4630–4639, https://doi.org/10.1039/C4DT03272A.

[24] S.H.A. Lee, N.M. Abrams, P.G. Hoertz, G.D. Barber, L.I. Halaoui, T.E. Mallouk, Coupling of titania inverse opals to nanocrystalline titania layers in dye-sensitized solar cells, J. Phys. Chem. B 112 (46) (2008) 14415–14421, https://doi.org/10.1021/jp802692u.

[25] D.L. Ashford, W. Song, J.J. Concepcion, C.R.K. Glasson, M.K. Brennaman, M. R. Norris, Z. Fang, J.L. Templeton, T.J. Meyer, Photoinduced electron transfer in a chromophore-catalyst assembly anchored to TiO_2, J. Am. Chem. Soc. 134 (46) (2012) 19189–19198, https://doi.org/10.1021/ja3084362.

[26] S.M. Zakeeruddin, Md.K. Nazeeruddin, R. Humphry-Baker, P. Péchy, P. Quagliotto, C. Barolo, G. Viscardi, M. Grätzel, Design, synthesis, and application of amphiphilic ruthenium polypyridyl photosensitizers in solar cells based on nanocrystalline TiO_2 films, Langmuir 18 (3) (2002) 952–954, https://doi.org/10.1021/la0110848.

[27] I Langmuir, The adsorption of gases on plane surfaces of glass, mica, and platinum, J. Am. Chem. Soc. 40 (9) (1918) 1361–1403, https://doi.org/10.1021/ja02242a004.

[28] O.O. Ogunsolu, A.J. Braun, A.J. Robb, S.R. Salpage, Y. Zhou, K. Hanson, Influence of dye-coordinated metal ions on electron transfer dynamics at dye-semiconductor interfaces, ACS Appl. Energy Mater. 2 (1) (2019) 29–36, https://doi.org/10.1021/acsaem.8b01559.

[29] A. Fillinger, B.A. Parkinson, The adsorption behavior of a ruthenium-based sensitizing dye to nanocrystalline TiO_2 coverage effects on the external and internal sensitization quantum yields, J. Electrochem. Soc. 146 (12) (1999) 4559–4564, https://doi.org/10.1149/1.1392674.

[30] Z.-.S. Wang, H. Sugihara, N3-sensitized TiO_2 films: *in situ* proton exchange toward open-circuit photovoltage enhancement, Langmuir 22 (23) (2006) 9718–9722, https://doi.org/10.1021/la061315g.

[31] K. Hanson, M.K. Brennaman, H. Luo, C.R.K. Glasson, J.J. Concepcion, W. Song, T. J. Meyer, Photostability of phosphonate-derivatized, Ru II polypyridyl complexes on metal oxide surfaces, ACS Appl. Mater. Interfaces 4 (3) (2012) 1462–1469, https://doi.org/10.1021/am201717x.

[32] A.J. Robb, E.S. Knorr, N. Watson, K. Hanson, Metal ion linked multilayers on mesoporous substrates: energy/electron transfer, photon upconversion, and more, J. Photochem. Photobiol. Chem. 390 (2020), 112291, https://doi.org/10.1016/j.jphotochem.2019.112291.

[33] J. Lin, Y. Li, B. Xie, Heterogeneous photocatalytic performances of CO_2 reduction based on the [Emim]BF_4 + TEOA + H_2O system, RSC Adv. 9 (61) (2019) 35841–35846, https://doi.org/10.1039/C9RA06235A.

[34] Md.K. Nazeeruddin, R. Humphry-Baker, P. Liska, M. Grätzel, Investigation of sensitizer adsorption and the influence of protons on current and voltage of a dye-sensitized nanocrystalline TiO_2 solar cell, J. Phys. Chem. B 107 (34) (2003) 8981–8987, https://doi.org/10.1021/jp022656f.

[35] A.J. Robb, D. Miles, S.R. Salpage, N. Watson, Q. He, Q. Wu, K. Hanson, Role of metal ion-linked multilayer thickness and substrate porosity in surface loading, diffusion, and solar energy conversion, ACS Appl. Mater. Interfaces 12 (34) (2020) 38003–38011, https://doi.org/10.1021/acsami.0c07968.

[36] C.C. Rich, M.A. Mattson, A.T. Krummel, Direct measurement of the absolute orientation of N_3 dye at gold and titanium dioxide surfaces with heterodyne-detected vibrational SFG spectroscopy, J. Phys. Chem. C 120 (12) (2016) 6601–6611, https://doi.org/10.1021/acs.jpcc.5b12649.

[37] O.O. Ogunsolu, J.C. Wang, K. Hanson, Increasing the Open-circuit voltage of dye-sensitized solar cells via metal-ion coordination, Inorg. Chem. 56 (18) (2017) 11168–11175, https://doi.org/10.1021/acs.inorgchem.7b01531.

[38] S.P. Hill, K. Hanson, Harnessing molecular photon upconversion in a solar cell at sub-solar irradiance: role of the redox mediator, J. Am. Chem. Soc. 139 (32) (2017) 10988–10991, https://doi.org/10.1021/jacs.7b05462.

[39] F. Fabregat-Santiago, G. Garcia-Belmonte, I. Mora-Seró, J. Bisquert, Characterization of nanostructured hybrid and organic solar cells by impedance spectroscopy, Phys. Chem. Chem. Phys. 9083 (20) (2011) 13, https://doi.org/10.1039/c0cp02249g.

[40] R. Katoh, A. Furube, T. Yoshihara, K. Hara, G. Fujihashi, S. Takano, S. Murata, H. Arakawa, M. Tachiya, Efficiencies of electron injection from excited N_3 Dye into nanocrystalline semiconductor (ZrO_2, TiO_2, ZnO, Nb_2O_5, SnO_2, In_2O_3) films, J. Phys. Chem. B 108 (15) (2004) 4818–4822, https://doi.org/10.1021/jp031260g.

[41] Y. Tachibana, J.E. Moser, M. Grätzel, D.R. Klug, J.R. Durrant, Subpicosecond interfacial charge separation in dye-sensitized nanocrystalline titanium dioxide films, J. Phys. Chem. 100 (51) (1996) 20056–20062, https://doi.org/10.1021/jp962227f.

[42] G. Benkö, J. Kallioinen, J.E.I. Korppi-Tommola, A.P. Yartsev, V. Sundström, Photoinduced ultrafast dye-to-semiconductor electron injection from nonthermalized and thermalized donor states, J. Am. Chem. Soc. 124 (3) (2002) 489–493, https://doi.org/10.1021/ja016561n.

[43] G. Benkö, J. Kallioinen, P. Myllyperkiö, F. Trif, J.E.I. Korppi-Tommola, A. P. Yartsev, V. Sundström, Interligand electron transfer determines triplet excited state electron injection in RuN_3-sensitized TiO_2 films, J. Phys. Chem. B 108 (9) (2004) 2862–2867, https://doi.org/10.1021/jp036778z.

[44] S. Ardo, G.J. Meyer, Direct Observation of photodriven intermolecular hole transfer across TiO_2 nanocrystallites: lateral self-exchange reactions and catalyst oxidation, J. Am. Chem. Soc. 132 (27) (2010) 9283–9285, https://doi.org/10.1021/ja1035946.

[45] H. Nusbaumer, J.-.E. Moser, S.M. Zakeeruddin, M.K. Nazeeruddin, M. Grätzel, $Co^{II}(Dbbip)_2^{2+}$ complex rivals tri-iodide/iodide redox mediator in dye-sensitized photovoltaic cells, J. Phys. Chem. B 105 (43) (2001) 10461–10464, https://doi.org/10.1021/jp012075a.

[46] S.A. Sapp, C.M. Elliott, C. Contado, S. Caramori, C.A. Bignozzi, Substituted polypyridine complexes of cobalt(II/III) as efficient electron-transfer mediators in dye-sensitized solar cells, J. Am. Chem. Soc. 124 (37) (2002) 11215–11222, https://doi.org/10.1021/ja027355y.

[47] K. Omata, S. Kuwahara, K. Katayama, S. Qing, T. Toyoda, K.M. Lee, C.G. Wu, The cause for the low efficiency of dye sensitized solar cells with a combination of ruthenium dyes and cobalt redox, Phys. Chem. Chem. Phys. 17 (15) (2015) 10170–10175, https://doi.org/10.1039/C4CP05981F.

[48] R.A. Marcus, On the theory of oxidation-reduction reactions involving electron transfer. I, J. Chem. Phys. 24 (5) (1956) 966–978, https://doi.org/10.1063/1.1742723.

[49] E.J. Piechota, G.J. Meyer, Introduction to electron transfer: theoretical foundations and pedagogical examples, J. Chem. Educ. 96 (11) (2019) 2450–2466, https://doi.org/10.1021/acs.jchemed.9b00489.

[50] S.M. Feldt, P.W. Lohse, F. Kessler, M.K. Nazeeruddin, M. Grätzel, G. Boschloo, A. Hagfeldt, Regeneration and recombination kinetics in cobalt polypyridine based dye-sensitized solar cells, explained using Marcus theory, Phys. Chem. Chem. Phys. 7087 (19) (2013) 15, https://doi.org/10.1039/c3cp50997d.

[51] E. Mosconi, J.-.H. Yum, F. Kessler, C.J. Gómez García, C. Zuccaccia, A. Cinti, M. K. Nazeeruddin, M. Grätzel, F. De Angelis, Cobalt electrolyte/dye interactions in dye-sensitized solar cells: a combined computational and experimental study, J. Am. Chem. Soc. 134 (47) (2012) 19438–19453, https://doi.org/10.1021/ja3079016.

[52] A. Arcidiacono, Y. Zhou, W. Zhang, J.O. Ellison, S. Ayad, E.S. Knorr, A.N. Peters, L. Zheng, W. Yang, S.S. Saavedra, K. Hanson, Examining the influence of bilayer structure on energy transfer and molecular photon upconversion in metal ion linked multilayers, J. Phys. Chem. C 124 (43) (2020) 23597–23610, https://doi.org/10.1021/acs.jpcc.0c08715.

[53] M.N. Paddon-Row, Investigating long-range electron-transfer processes with rigid, covalently linked donor-(Norbornylogous bridge)-acceptor systems, Acc. Chem. Res. 27 (1) (1994) 18–25, https://doi.org/10.1021/ar00037a003.

[54] D. Hanss, M.E. Walther, O.S. Wenger, Importance of covalence, conformational effects and tunneling-barrier heights for long-range electron transfer: insights from dyads with oligo-p-phenylene, oligo-p-xylene and oligo-p-dimethoxybenzene bridges, Coord. Chem. Rev. 254 (21) (2010) 2584–2592, https://doi.org/10.1016/j.ccr.2009.10.024.

[55] W.B. Davis, W.A. Svec, M.A. Ratner, M.R. Wasielewski, Molecular-wire behaviour in p -phenylenevinylene oligomers, Nature 396 (6706) (1998) 60–63, https://doi.org/10.1038/23912.

[56] J.C. Wang, K. Violette, O.O. Ogunsolu, K. Hanson, Metal ion mediated electron transfer at dye-semiconductor interfaces, Phys. Chem. Chem. Phys. 19 (4) (2017) 2679–2682, https://doi.org/10.1039/C6CP07939C.

[57] J.C. Wang, O.O. Ogunsolu, M. Sykora, K. Hanson, Elucidating the role of the metal linking ion on the excited state dynamics of self-assembled bilayers, J. Phys. Chem. C 122 (18) (2018) 9835–9842, https://doi.org/10.1021/acs.jpcc.8b02387.

[58] J.C. Wang, K. Violette, O.O. Ogunsolu, S. Cekli, E. Lambers, H.M. Fares, K. Hanson, Self-assembled bilayers on nanocrystalline metal oxides: exploring the non-innocent nature of the linking ions, Langmuir 33 (38) (2017) 9609–9619, https://doi.org/10.1021/acs.langmuir.7b01964.